International Forum on Aeroelasticity and Structural Dynamics
IFASD 2024
17-21 June 2024, The Hague, The Netherlands

NONLINEAR AEROELASTIC MODELLING OF ROTATING WIND BLADES

MENG Yang[1], XIE Changchuan[2]

[1] Flying College, Beihang University, 100191, Beijing, China, summy@buaa.edu.cn
[2] School of Aeronautic Science and Engineering, Beihang University, 100191, Beijing, China, xiechangc@buaa.edu.cn

Keywords: wind turbine blade, large deformation, nonlinear aeroelasticity

Abstract: The large wind turbine blades, while enhancing the efficiency of wind energy capture, inevitably lead to more complex nonlinear aeroelastic problems. This work aims to establish a nonlinear aeroelastic model for wind turbine blades by coupling strain-based beam with rotational effects and finite-state inflow theory with Prandtl tip loss correction. Numerical studies were conducted on a real blade model and compared with measured data.

1 INTRODUCTION

The trend in the offshore wind turbine industry is towards more energy harvesting capacity, resulting in larger and more flexible structural components for these huge rotating machines. These large flexible structures must withstand aerodynamic, hydrodynamic, gravitational, and geotechnical loads while in service due to their installation in harsh environments[1].

The flexible blades make aeroelasticity becomes one of the most critical issues during the design of modern wind turbines. To study the aeroelastic characteristics of wind turbine blades, various models with varying complexity are used at different design stages[2]. Mostly, at the component level beam models are used while at the complete wind turbine level, modal and multi-body approaches are usually adopted[3]. As for aerodynamic aspects, the Beddoes -Leishman (B-L) dynamic stall model is often used for predicting the aerodynamic loads in stall conditions [4]. Besides, researchers also utilize generalized dynamic wake (GDW) and unsteady vortex lattice method to consider the corresponding dynamic inflow effects[5]. The aerodynamic force and structural components together constitute the basis of fluid-solid interaction (FSI) modelling techniques. The most widely used aeroelastic model is based on the blade element momentum (BEM) theory and 1D beam structural models due to their high efficiency and reasonable accuracy.

However, one prominent feature of the large wind turbine blades is the large deformation during service, which can cause geometrically nonlinearities. Besides, researchers have found that unstable oscillations are more likely to occur with longer blades. Volk et al.[6] found that blades can exhibit edgewise instabilities beyond a critical rotor speed by field tests and simulation on a 7 MW wind turbine. The large flapwise deflections lead to coupling between the edgewise motion of the blade and its torsional motion, and further induce edgewise instabilities due to the reduction of the damping in the edgewise direction[7]. Zhou et al. [8] showed that nonlinear analysis predicts both flutter and edgewise non-flutter instabilities, while only flutter instability can be detected in linear analysis.

In this work, the authors will develop a nonlinear aeroelastic model for wind turbine blades by coupling strain-based beam with the finite-state inflow theory. Some experimental data from wind energy company indicate that the blades exhibit typical edgewise oscillations. Numerical studies are conducted to investigate the oscillations through aeroelastic simulations under conditions similar to measured data.

2 THEORETICAL FORMULATION

2.1 Coordinate system definition

As shown in Fig. 1, the base vector $\mathbf{E}_3$ of the reference coordinate system E is pointing upwards along the wind turbine frame. $\mathbf{E}_1$ is perpendicular to the rotation plane with zero inclination and cone angle. Denote the inclination angle of the rotation plane as φ, the cone angle as θ. The rotation matrix from the reference coordinate system E to the body coordinate system B can be expressed by

$$\boldsymbol{C}^{BE} = \boldsymbol{L}_y(\theta)\boldsymbol{L}_x(\Omega t)\boldsymbol{L}_y(\varphi) \tag{1}$$\

where Ω is the rotational speed and $\boldsymbol{L}_x(\phi), \boldsymbol{L}_y(\theta), \boldsymbol{L}_z(\psi)$ are the Euler rotation matrix denoted by

$$\boldsymbol{L}_x(\phi) = \begin{bmatrix} 1 & 0 & 0 \\ 0 & \cos\phi & \sin\phi \\ 0 & -\sin\phi & \cos\phi \end{bmatrix}, \boldsymbol{L}_y(\theta) = \begin{bmatrix} \cos\theta & 0 & -\sin\theta \\ 0 & 1 & 0 \\ \sin\theta & 0 & \cos\theta \end{bmatrix}, \boldsymbol{L}_z(\psi) = \begin{bmatrix} \cos\psi & \sin\psi & 0 \\ -\sin\psi & \cos\psi & 0 \\ 0 & 0 & 1 \end{bmatrix} \tag{2}$$

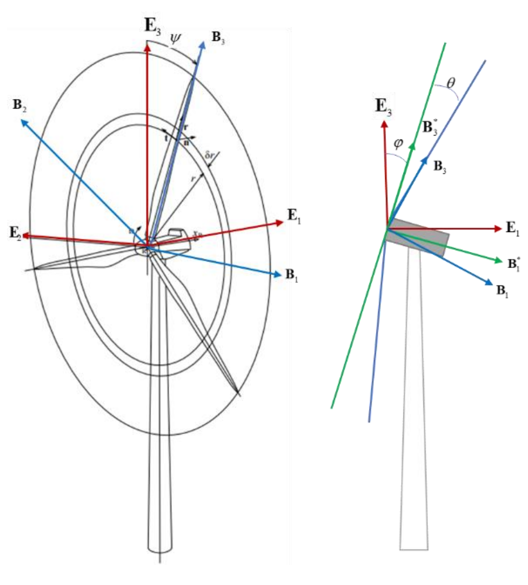

Fig. 1 Coordinate system definition

2.2 Structural modelling of rotating beam

A rotating beam, as shown in Fig. 2, is defined by a spatial curve parameterized with the arc length coordinate $s \in [0, L] \subset \mathbb{R}$ and a family of cross-sections.

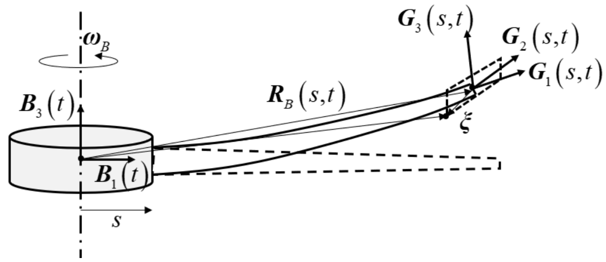

Fig. 2 Kinematic description of a rotating beam

For a balanced system, the sum of the virtual work done by all inertial forces, elastic forces, and external forces on possible virtual displacements is zero：

$$\int_0^L \left(\delta W_a + \delta W_\varepsilon + \delta W_e \right) ds = 0 \tag{3}$$

in which, δW_a, δW_ε and δW_e are the virtual work of inertial force, elastic force and external force per unit length, respectively. The key to derive these virtual works is to determine the kinematic relations. The rotating frame B rotates around the $\mathbf{B}_3(t)$ axis at an angular velocity of $\boldsymbol{\omega}_B$.Assuming that the inertial reference frame E coincides with the rotating frame B at the initial time, the position vector of an arbitrary point P in the beam can be expressed as

$${}^P\mathbf{R}_E(s,t) = \mathbf{C}^{EB}(t)\left[\mathbf{R}_B(s,t) + \xi_1 \mathbf{G}_{1,B}(s,t) + \xi_2 \mathbf{G}_{2,B}(s,t) + \xi_3 \mathbf{G}_{3,B}(s,t) \right] \tag{4}$$

where $\mathbf{R}_B(s,t)$ is the position vector of the origin of the local coordinate system G, and $\boldsymbol{\xi}_G = \begin{bmatrix} \xi_1 & \xi_2 & \xi_3 \end{bmatrix}^T$ is the position vector of the point P in the local frame G. With the assumption that the cross-section is rigid, the vector $\boldsymbol{\xi}_G$ remains constant. The subscripts here indicate that these vectors' components are expressed in the corresponding coordinate systems.

Similar to Ref.[10], the nodal position and orientation information within the rotating frame can be denoted as：

$$\mathbf{q}(s,t) = \begin{bmatrix} \mathbf{R}_B^T(s,t) & \mathbf{G}_{1,B}^T(s,t) & \mathbf{G}_{2,B}^T(s,t) & \mathbf{G}_{3,B}^T(s,t) \end{bmatrix}^T \tag{5}$$

Accordingly，the position vector ${}^P\mathbf{R}_E(s,t)$ can be expressed as：

$$ {}^{P}\mathbf{R}_{E}\left(s,t\right)=\mathbf{C}^{EB}\left(t\right)\boldsymbol{\Gamma}\mathbf{q}\left(s,t\right) \tag{6} $$

in which $\boldsymbol{\Gamma}=\left[\boldsymbol{\Delta} \quad \xi_1\boldsymbol{\Delta} \quad \xi_2\boldsymbol{\Delta} \quad \xi_3\boldsymbol{\Delta}\right]$ and $\boldsymbol{\Delta}$ is a 3 by 3 unit matrix. The velocity and acceleration of the point P can be calculated by taking time derivatives of the position vector ${}^{P}\mathbf{R}_{E}\left(s,t\right)$:

$$ \begin{aligned} {}^{P}\mathbf{V}_{B}\left(s,t\right)&=\tilde{\boldsymbol{\omega}}_{B}\left(t\right)\boldsymbol{\Gamma}\dot{\mathbf{q}}\left(s,t\right)+\boldsymbol{\Gamma}\dot{\mathbf{q}}\left(s,t\right) \\ {}^{P}\mathbf{a}_{B}\left(s,t\right)&=\dot{\tilde{\boldsymbol{\omega}}}_{B}\boldsymbol{\Gamma}\mathbf{q}\left(s,t\right)+\tilde{\boldsymbol{\omega}}_{B}\tilde{\boldsymbol{\omega}}_{B}\boldsymbol{\Gamma}\mathbf{q}\left(s,t\right)+2\tilde{\boldsymbol{\omega}}_{B}\boldsymbol{\Gamma}\dot{\mathbf{q}}\left(s,t\right)+\boldsymbol{\Gamma}\ddot{\mathbf{q}}\left(s,t\right) \end{aligned} \tag{7} $$

in which, the angular velocity $\boldsymbol{\omega}_{B}$ of the body frame satisfies $\tilde{\boldsymbol{\omega}}_{B}\left(t\right)=\mathbf{C}^{BE}\dot{\mathbf{C}}^{EB}$.
The virtual work of the inertial force per unit length is

$$ \delta W_{a}=-\int_{A(s)}\delta\left({}^{P}\mathbf{R}_{E}^{T}\right)\mathbf{C}^{EB}\left({}^{P}\mathbf{a}_{B}\right)\rho dA \tag{8} $$

in which, $A\left(s\right)$ is the cross-sectional aera and ρ is the mass density.

The virtual work of the elastic force per unit length is

$$ \delta W_{\varepsilon}=-\delta\boldsymbol{\gamma}^{T}\mathbf{F}_{G}-\delta\boldsymbol{\kappa}^{T}\mathbf{M}_{G}=-\left[\delta\boldsymbol{\gamma}^{T} \quad \delta\boldsymbol{\kappa}^{T}\right]\mathbf{S}_{cs}\left[\boldsymbol{\gamma}^{T} \quad \boldsymbol{\kappa}^{T}\right]^{T} \tag{9} $$

in which, $\boldsymbol{\gamma}=\left[\gamma_{11} \quad 2\gamma_{12} \quad 2\gamma_{13}\right]^{T}$ represents the force strain composed of tensile strain and shear strain, which physically describes the difference between the tangent vectors of the beam reference line before and after deformation pulled back to the material coordinate system (local coordinate system) and is used to describe the deformation of the beam section. $\boldsymbol{\kappa}=\left[\kappa_{1} \quad \kappa_{2} \quad \kappa_{3}\right]^{T}$ represents the moment strain composed of torsional and bending curvature, which physically describes the overall deformation of the beam reference line. $\mathbf{S}_{cs}$ is the cross-sectional stiffness matrix.

The virtual work of the external force per unit length is

$$ \delta W_{e}=\int_{A(s)}\delta\left({}^{P}\mathbf{R}_{E}^{T}\right)\mathbf{X}_{E}dA=\delta\boldsymbol{\varphi}_{B}^{T}\left(\tilde{\mathbf{R}}_{B}\mathbf{f}_{B}+\mathbf{m}_{B}\right)+\delta\mathbf{R}_{B}^{T}\mathbf{f}_{B}+\delta\boldsymbol{\Theta}_{B}^{T}\mathbf{m}_{B} \tag{10} $$

in which, $\mathbf{X}_{E}$ is the body force. $\delta\boldsymbol{\varphi}_{B}$ and $\delta\boldsymbol{\Theta}_{B}$ are the infinitesimal rotation vectors and $\delta\tilde{\boldsymbol{\varphi}}_{B}=\mathbf{C}^{BE}\delta\mathbf{C}^{EB}, \delta\tilde{\boldsymbol{\Theta}}_{B}=\delta\mathbf{C}^{BG}\mathbf{C}^{GB}$. $\mathbf{f}_{B}$ and $\mathbf{m}_{B}$ are the external forces and moments, respectively.

Substituting Eqs.(8)-(10) into Eq. (3) and yields,

$$\int_0^L \left(\delta W_a + \delta W_\varepsilon + \delta W_e\right) ds = \int_0^L \begin{pmatrix} -\delta \mathbf{q}^T \left(\mathbf{M}_{cs}\ddot{\mathbf{q}} + 2\mathbf{M}_{cs}\mathbf{\Pi}_B\dot{\mathbf{q}} + \mathbf{M}_{cs}\mathbf{\Pi}_B\tilde{\tilde{\mathbf{q}}}\boldsymbol{\omega}_B\right) \\ -\delta\boldsymbol{\varphi}_B^T\left(\tilde{\tilde{\mathbf{q}}}^T\mathbf{M}_{cs}\ddot{\mathbf{q}} + 2\tilde{\tilde{\mathbf{q}}}^T\mathbf{M}_{cs}\mathbf{\Pi}_B\dot{\mathbf{q}} + \tilde{\tilde{\mathbf{q}}}^T\mathbf{M}_{cs}\mathbf{\Pi}_B\tilde{\tilde{\mathbf{q}}}\boldsymbol{\omega}_B\right) \\ -\delta\boldsymbol{\gamma}^T\mathbf{F}_G - \delta\boldsymbol{\kappa}^T\mathbf{M}_G + \delta\boldsymbol{\varphi}_B^T\left(\tilde{\mathbf{R}}_B\mathbf{f}_B + \mathbf{m}_B\right) + \delta\mathbf{R}_B^T\mathbf{f}_B + \delta\mathbf{\Theta}_B^T\mathbf{m}_B \end{pmatrix} ds = 0 \tag{11}$$

in which, $\mathbf{M}_{cs}(s) = \int_{A(s)} \rho \mathbf{\Gamma}^T \mathbf{\Gamma} dA$ represents the cross-sectional mass property. $\tilde{\tilde{\mathbf{q}}}$ and $\mathbf{\Pi}_B$ are defined by

$$\tilde{\tilde{\mathbf{q}}} = \begin{bmatrix} \tilde{\mathbf{R}}_B^T \\ \tilde{\mathbf{G}}_{1,B}^T \\ \tilde{\mathbf{G}}_{2,B}^T \\ \tilde{\mathbf{G}}_{3,B}^T \end{bmatrix}, \quad \mathbf{\Pi}_B = \begin{bmatrix} \tilde{\boldsymbol{\omega}}_B & & & \\ & \tilde{\boldsymbol{\omega}}_B & & \\ & & \tilde{\boldsymbol{\omega}}_B & \\ & & & \tilde{\boldsymbol{\omega}}_B \end{bmatrix} \tag{12}$$

Eq. (11) can be decomposed into two parts: the external force balance equation and the internal force balance equation.

$$\delta\boldsymbol{\varphi}_B^T \int_0^L \left[\tilde{\mathbf{R}}_B\mathbf{f}_B + \mathbf{m}_B - \left(\tilde{\tilde{\mathbf{q}}}^T\mathbf{M}_{cs}\ddot{\mathbf{q}} + 2\tilde{\tilde{\mathbf{q}}}^T\mathbf{M}_{cs}\mathbf{\Pi}_B\dot{\mathbf{q}} + \tilde{\tilde{\mathbf{q}}}^T\mathbf{M}_{cs}\mathbf{\Pi}_B\tilde{\tilde{\mathbf{q}}}\boldsymbol{\omega}_B\right)\right] ds = 0 \tag{13}$$

$$\int_0^L \left(-\delta\mathbf{q}^T\left(\mathbf{M}_{cs}\ddot{\mathbf{q}} + 2\mathbf{M}_{cs}\mathbf{\Pi}_B\dot{\mathbf{q}} + \mathbf{M}_{cs}\mathbf{\Pi}_B\tilde{\tilde{\mathbf{q}}}\boldsymbol{\omega}_B\right) - \delta\boldsymbol{\gamma}^T\mathbf{F}_G - \delta\boldsymbol{\kappa}^T\mathbf{M}_G + \delta\mathbf{R}_B^T\mathbf{f}_B + \delta\mathbf{\Theta}_B^T\mathbf{m}_B\right) ds = 0 \tag{14}$$

In this work, we assume the angular velocity is given, which means that Eq.(13) is automatically satisfied. Eq. (14) is then solved by finite-element analysis.

The beam can be discretized into N elements with constant strains, which yields the strain vector of the i-th element

$$\boldsymbol{\varepsilon}_i = \begin{bmatrix}\boldsymbol{\gamma}_i^T & \boldsymbol{\kappa}_i^T\end{bmatrix}^T = \begin{bmatrix}\gamma_{11,i} & 2\gamma_{12,i} & 2\gamma_{13,i} & \kappa_{1,i} & \kappa_{2,i} & \kappa_{3,i}\end{bmatrix}^T \tag{15}$$

and we have $\bar{\boldsymbol{\varepsilon}} = \begin{bmatrix}\boldsymbol{\varepsilon}_1^T & \boldsymbol{\varepsilon}_2^T & \cdots & \boldsymbol{\varepsilon}_i^T & \cdots & \boldsymbol{\varepsilon}_N^T\end{bmatrix}^T$. According to Ref [10], $\delta\bar{\mathbf{q}}$, $\delta\bar{\mathbf{R}}_B$ and $\delta\bar{\mathbf{\Theta}}_B$ can be related to $\delta\bar{\boldsymbol{\varepsilon}}$ by

$$\begin{aligned} &\delta\bar{\mathbf{q}} = \mathbf{J}_{q\varepsilon}\delta\bar{\boldsymbol{\varepsilon}}, \ \delta\bar{\mathbf{R}}_B = \mathbf{J}_{R\varepsilon}\delta\bar{\boldsymbol{\varepsilon}}, \ \delta\bar{\mathbf{\Theta}}_B = \mathbf{J}_{\Theta\varepsilon}\delta\bar{\boldsymbol{\varepsilon}} \\ &\dot{\bar{\mathbf{q}}} = \mathbf{J}_{q\varepsilon}\dot{\bar{\boldsymbol{\varepsilon}}} \\ &\ddot{\bar{\mathbf{q}}} = \mathbf{J}_{q\varepsilon}\ddot{\bar{\boldsymbol{\varepsilon}}} + \dot{\mathbf{J}}_{q\varepsilon}\dot{\bar{\boldsymbol{\varepsilon}}} \end{aligned} \tag{16}$$

in which $\mathbf{J}_{q\varepsilon}$, $\mathbf{J}_{R\varepsilon}$ and $\mathbf{J}_{\Theta\varepsilon}$ are the Jacobian matrices.

By piecewise integration of Eq. (14), one can finally obtain the discretized dynamic equilibrium equation

$$\mathbf{J}_{\mathbf{q}\boldsymbol{\varepsilon}}^T\mathbf{M}\mathbf{J}_{\mathbf{q}\boldsymbol{\varepsilon}}\ddot{\bar{\boldsymbol{\varepsilon}}} + \mathbf{J}_{\mathbf{q}\boldsymbol{\varepsilon}}^T\mathbf{M}\left(\dot{\mathbf{J}}_{\mathbf{q}\boldsymbol{\varepsilon}} + 2\mathbf{\Xi}_B\mathbf{J}_{\mathbf{q}\boldsymbol{\varepsilon}}\right)\dot{\bar{\boldsymbol{\varepsilon}}} + \mathbf{J}_{\mathbf{q}\boldsymbol{\varepsilon}}^T\mathbf{M}\mathbf{\Xi}_B\mathbf{\Xi}_B\bar{\mathbf{q}} + \mathbf{K}\bar{\boldsymbol{\varepsilon}} = \mathbf{K}\bar{\boldsymbol{\varepsilon}}_0 + \mathbf{J}_{\mathbf{R}\boldsymbol{\varepsilon}}^T\bar{\mathbf{f}}_B + \mathbf{J}_{\mathbf{\Theta}\boldsymbol{\varepsilon}}^T\bar{\mathbf{m}}_B \tag{17}$$

in which,

$$\mathbf{M}=\begin{bmatrix}\mathbf{M_{e1}} & & & \\ & \mathbf{M_{e2}} & & \\ & & \ddots & \\ & & & \mathbf{M_{eN}}\end{bmatrix},\boldsymbol{\Xi}_B=\begin{bmatrix}\boldsymbol{\Pi}_B & & & \\ & \boldsymbol{\Pi}_B & & \\ & & \ddots & \\ & & & \boldsymbol{\Pi}_B\end{bmatrix},\mathbf{K}=\begin{bmatrix}\Delta s_1\mathbf{S}_{cs1} & & & \\ & \Delta s_2\mathbf{S}_{cs2} & & \\ & & \ddots & \\ & & & \Delta s_N\mathbf{S}_{csN}\end{bmatrix}$$

(18)

2.3 Unsteady aerodynamics based on finite-state inflow theory

Aerodynamic loads are calculated by the two-dimensional finite-state inflow theory and the Prandtl blade tip loss model is used for spanwise correction. The theory provides aerodynamic forces on a thin airfoil undergoing large motions in an incompressible flow. The lift L and moment $M_{1/4}$ of a thin 2-D airfoil are expressed by

$$\begin{cases} L=\pi\rho_\infty b^2\left(\ddot{h}+U\dot{\theta}-ba\ddot{\theta}\right)+2\pi\rho_\infty Ub\left[\dot{h}+U\theta+b\left(\dfrac{1}{2}-a\right)\dot{\theta}-\lambda_0\right] \\ M_{1/4}=-\pi\rho_\infty b^3\left[\dfrac{1}{2}\ddot{h}+U\dot{\theta}+b\left(\dfrac{1}{8}-\dfrac{a}{2}\right)\ddot{\theta}\right] \end{cases} \tag{19}$$

in which b is the semi-chord, ba is the distance of the mid-chord in front of the reference axis, ρ_∞ is the airflow density and U is airflow speed. With regard to airfoil motions, h represents the plunging motion and θ represents the pitching motion. The inflow parameter λ_0 accounts for induced flow due to free velocity. Consider N induced-flow states:

$$\lambda_0\approx\frac{1}{2}\sum_{n=1}^{N}b_n\lambda_n \tag{20}$$

where b_n are calculated by the least-squares method. The governed equation of inflow states is

$$\mathbf{A}\dot{\boldsymbol{\lambda}}+\frac{U}{b}\boldsymbol{\lambda}=\mathbf{c}\left[\ddot{h}+U\dot{\theta}+b\left(\frac{1}{2}-a\right)\ddot{\theta}\right] \tag{21}$$

The matrices $\mathbf{A}$ and $\mathbf{c}$ are given described in Ref. [12] and $\boldsymbol{\lambda}=\begin{bmatrix}\lambda_1 & \lambda_2 & \cdots & \lambda_N\end{bmatrix}^T$.

According to the kinematic relations described in Fig. 3, the speed of plunging motion and pitching motion, the airflow speed can be expressed in terms of the structural motion and free inflow velocity,

$$\begin{aligned} \dot{h}&=-\mathbf{i}_{2,B}^T\left(\mathbf{J}_{\mathbf{R\varepsilon}}\dot{\boldsymbol{\varepsilon}}\right) \\ \dot{\theta}&=\mathbf{i}_{3,B}^T\left(\mathbf{J}_{\boldsymbol{\varphi}\boldsymbol{\varepsilon}}\dot{\boldsymbol{\varepsilon}}\right) \\ U&=-\mathbf{i}_{1,B}^T\left(\mathbf{U}_B-\mathbf{J}_{\mathbf{R\varepsilon}}\dot{\boldsymbol{\varepsilon}}\right) \end{aligned} \tag{22}$$

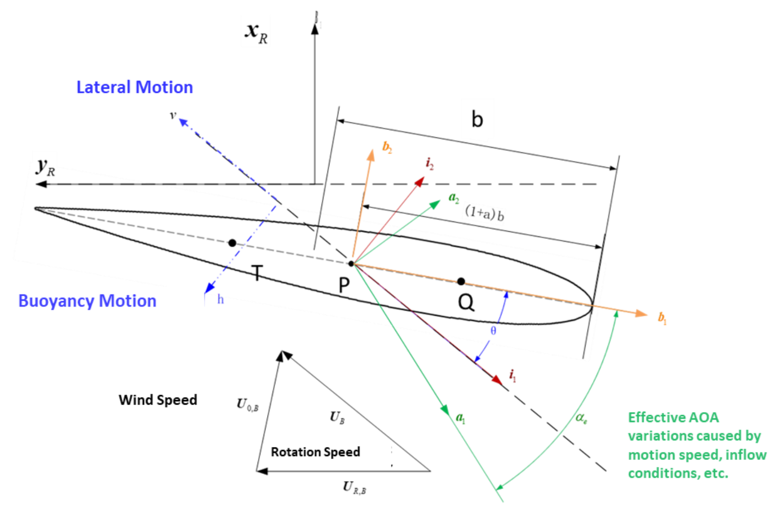

Fig. 3 Kinematics of the two-dimensional airfoil

The effect of the tip loss is modelled using Prandtl's theory that is used widely for aeroelastic simulations of turbines. The main result is summarized in the Prandtl's tip loss factor F by the equation

$$F = \frac{2}{\pi} \arccos\left(e^{-f_w}\right) \tag{23}$$

where

$$f_w = \frac{B}{2}\left(\frac{R-r}{r \sin\varphi}\right) \tag{24}$$

Here B is the number of blades, R is the rotor radius, r is the local radius of the blade element, while φ is the inflow angle.

2.4 Nonlinear aeroelastic formulation

The governed equation of inflow states can be expressed in terms of strain vector:

$$\dot{\boldsymbol{\lambda}} = \mathbf{Q}_1 \ddot{\boldsymbol{\varepsilon}} + \mathbf{Q}_2 \dot{\boldsymbol{\varepsilon}} + \mathbf{Q}_3 \boldsymbol{\lambda} \tag{25}$$

in which,

$$\begin{gathered} \mathbf{Q}_1 = \mathbf{A}^{-1}\left[-c\mathbf{i}_{3,B}^T \mathbf{J}_{\mathbf{R\varepsilon}} + b\left(\frac{1}{2} - a\right)\mathbf{i}_{1,B}^T \mathbf{J}_{\boldsymbol{\varphi\varepsilon}} \right] \\ \mathbf{Q}_2 = \mathbf{A}^{-1} \mathbf{c} U \mathbf{i}_{1,B}^T \mathbf{J}_{\boldsymbol{\varphi\varepsilon}}, \mathbf{Q}_3 = -\mathbf{A}^{-1}\frac{U}{b} \end{gathered} \tag{26}$$

Combining Eqs.(17) and (25), we have the formulation of nonlinear aeroelastic system：

$$\begin{cases} \mathbf{J}_{\mathbf{q}\varepsilon}^{T}\mathbf{M}\mathbf{J}_{\mathbf{q}\varepsilon}\ddot{\boldsymbol{\varepsilon}} + \mathbf{J}_{\mathbf{q}\varepsilon}^{T}\mathbf{M}\left(\dot{\mathbf{J}}_{\mathbf{q}\varepsilon} + 2\boldsymbol{\Xi}_{B}\mathbf{J}_{\mathbf{q}\varepsilon}\right)\dot{\boldsymbol{\varepsilon}} + \mathbf{J}_{\mathbf{q}\varepsilon}^{T}\mathbf{M}\boldsymbol{\Xi}_{B}\boldsymbol{\Xi}_{B}\bar{\mathbf{q}} + \mathbf{K}\bar{\boldsymbol{\varepsilon}} = \mathbf{K}\bar{\boldsymbol{\varepsilon}}_{0} + \mathbf{J}_{\mathbf{R}\varepsilon}^{T}\bar{\mathbf{f}}_{B} + \mathbf{J}_{\boldsymbol{\Theta}\varepsilon}^{T}\bar{\mathbf{m}}_{B} \\ \dot{\boldsymbol{\lambda}} = \mathbf{Q}_{1}\ddot{\boldsymbol{\varepsilon}} + \mathbf{Q}_{2}\dot{\boldsymbol{\varepsilon}} + \mathbf{Q}_{3}\boldsymbol{\lambda} \end{cases} \tag{27}$$

The above equations will be solved using the implicit Newmark integration scheme incorporating Newton-Raphson iterations for solving nonlinear equations[13]. The basic idea is to firstly provide the predictions of the state variables and their time derivatives at each time step and employ a Newton-Raphson sub-iteration technique to correct the predictions. The overall flowchart of time response simulation for wind turbine blade is shown in Fig. 4.

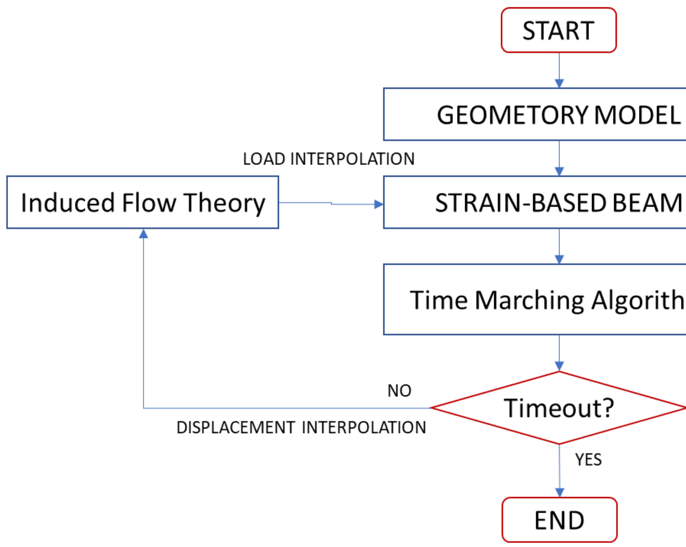

Fig. 4 Time response simulation flowchart

3 RESULTS AND ANALYSIS

3.1 Model description

A real wind turbine blade with length of 87 meters is modelled and analyzed. The CAD model is shown in Fig. 5. Cross-sectional properties were extracted firstly to form the beam model. Table 1 lists the modal results, followed by the first four mode shapes depicted in Fig. 6.

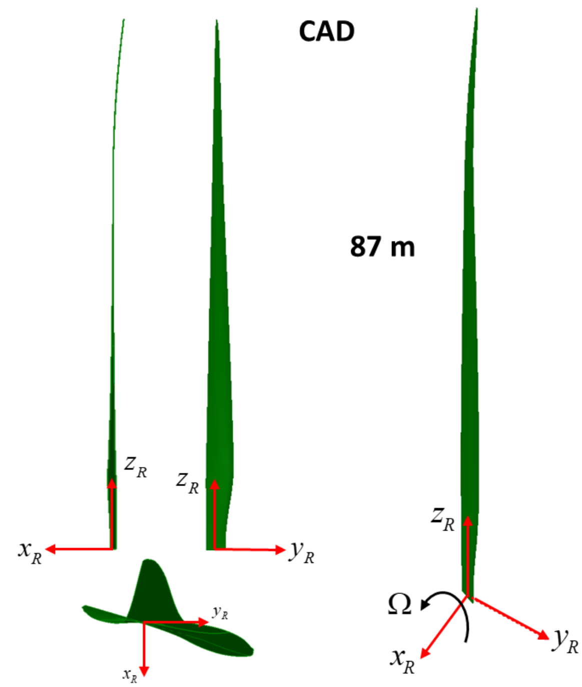

Fig. 5 CAD model of the wind turbine blade

Table 1 Modal results

No.	Modal shape	Mode freq.（Hz）
1	1^{st} Vertical bend	0.392
2	1^{st} Inplane bend	0.615
3	2^{nd} Vertical bend	1.028
4	2^{nd} Inplane bend	1.552
11	1^{st} Torsion	5.562

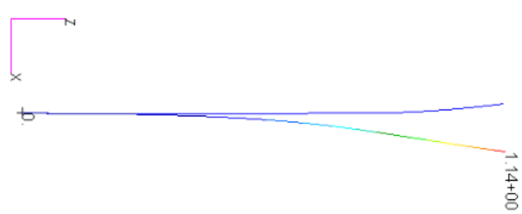

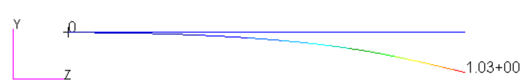

(a) 1^{st} vertical bend (b) 1^{st} inplane bend

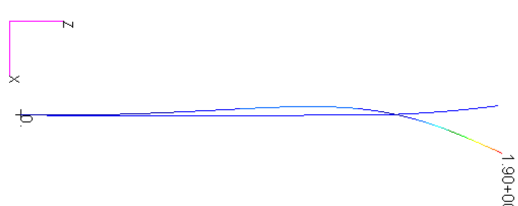

(c)2^{nd} vertical bend (d) 2^{nd} inplane bend

Fig. 6 The first four mode shapes

3.2 Measured data

Fig. 7 and 8(a) respectively show the time series data of blade rotation speed and root bending moments monitored by a wind energy company. The fan starts to work after about 40,000 s. Figure 8(b) shows the time period from 50,000 s to 60,000 s, in which the blue line represents the edgewise moment about the x-axis and the red line represents the flapping moment about the y-axis. The blade rotation speed within this time period is approximately stable near 10 RPM. Fig. 9 shows the fast Fourier transform (FFT) results of time-domain response of moment from 50000s to 60000s. The steady-state moment component corresponding to a frequency of zero is mainly the flapping moment, with an amplitude of 1.46e7 N·m. While the moment component corresponding to a frequency of 0.17 Hz is mainly the edgewise moment, with an amplitude of 1.89e6 N·m. The wind speed during the operation of the blade in this time period is approximately 10-15 m/s, as shown in Fig. 10. It can be found that the blade suffered an unexpected edgewise oscillation during normal operation. This may have an impact on the structural safety and fatigue characteristics of the blade. Next, we will try to reproduce this process through numerical simulation and investigate the influence of various parameters on the blade oscillations.

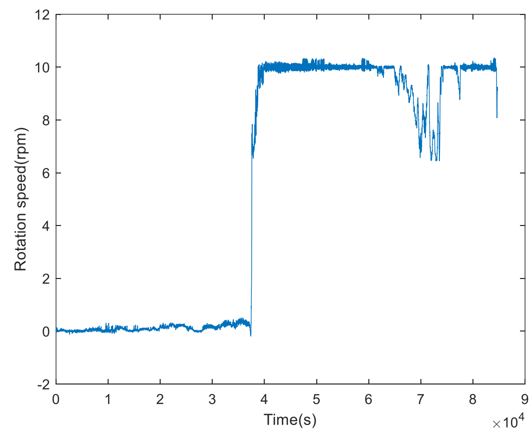

Fig. 7 Blade rotation speed

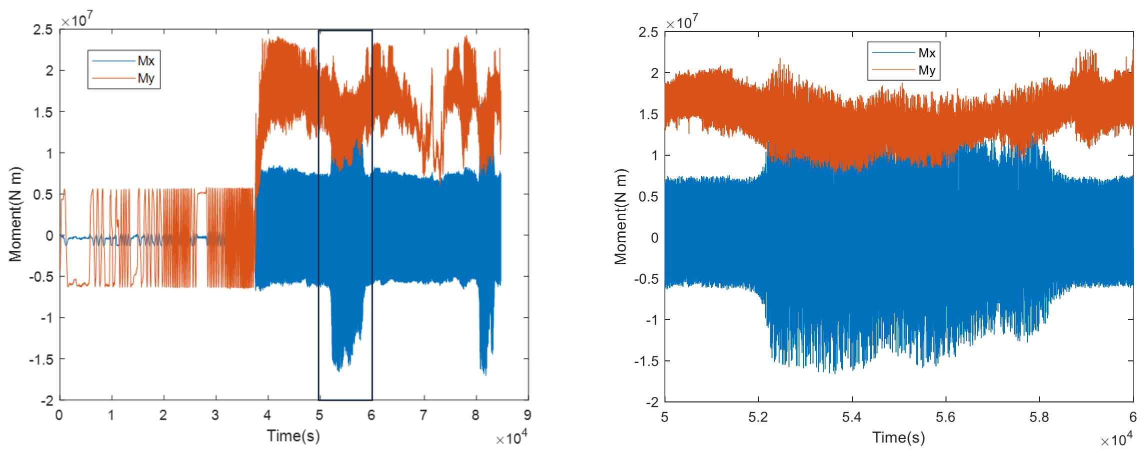

（a）Time series of moment **(b)Time series of moment from 50000s to 60000s**

Fig. 8 Time series of bending moments

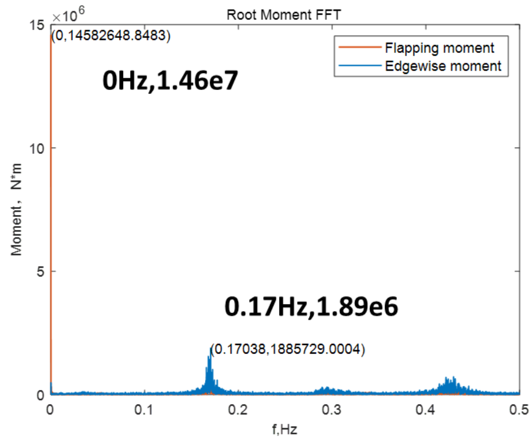

Fig. 9 FFT results of time-domain response of moment from 50000s to 60000s

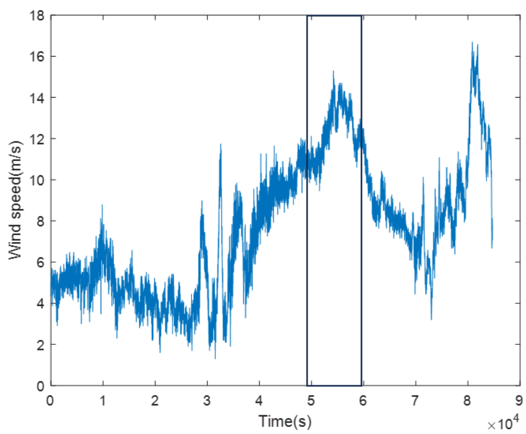

Fig. 10 Wind speed

3.3 Numerical simulation

Based on the measured data, the simulation parameters are set as listed in Table 2. The blade rotation speed is always 10 rpm. Two typical wind speeds have been selected from 10 to 15 m/s: 12 m/s and 14 m/s. The wind angle refers to the angle between the wind speed and the horizontal ground. The inclination angle and the cone angle have been defined in Section 2.1. The pitch angle is the angle between the chord line of the blade cross section and the rotating plane. The yaw angle is the angle between the wind speed and the rotating plane.

Table 2 Simulation parameters

No.	Rotation Speed	Wind Speed	Wind Angle	Cone Angle	Inclination Angle	Pitch Angle	Yaw Angle
CASE1	10rpm	14 m/s	8°	6°	6°	9°	0°
CASE2		14 m/s				9°	-8°
CASE3		12 m/s				4°	0°
CASE4		12 m/s				6°	0°
CASE5		14 m/s				9°	8°

Taking CASE1 as an example, Fig. 11(a)-Fig. 13(a) respectively plot the time-domain response curves of the root bending moment, the aerodynamic resultant force, and the tip displacement. All curves have a periodic response consistent with the rotational frequency. The flapping moment and the edgewise moment are much larger than the torsional moment, which is consistent with the distribution of the aerodynamic force. The aerodynamic force in the X direction is the largest, generating the flapping moment. The x-direction deformation of the tip is approximately at the order of 10 meters, which is about 11.5% of the length. By FFT analysis, the frequency-domain results are obtained and as shown in Fig. 11(b)-Fig. 13(b). The amplitudes corresponding to the frequency of 0Hz are listed in Table 3, and the amplitudes corresponding to the frequency of 0.17 Hz are listed in Table 4. It can be observed that:

1) The steady-state moment component corresponding to a frequency of zero is mainly the flapping moment. The amplitudes are pretty close to the measured data 1.46e7 N·m. While the moment components corresponding to a frequency of 0.17 Hz are much higher than the measured edgewise moments. The error may be due to the inconsistency between the input parameters and the actual situation. All in all, the numerical results can to some extent capture the atypical vibration characteristics of flexible blades.

2) When there is a yaw angle, the average flapwise displacement response decreases regardless of whether it is positive or negative.

3)As the yaw angle changes from negative to positive, the flapwise displacement response amplitude increases at 0.17Hz, while the edgewise displacement response amplitude decreases.

4)As the pitch angle increases, the displacement response levels in all directions decrease.

5)The pitch angle has a more significant effect than the wind speed on the load.

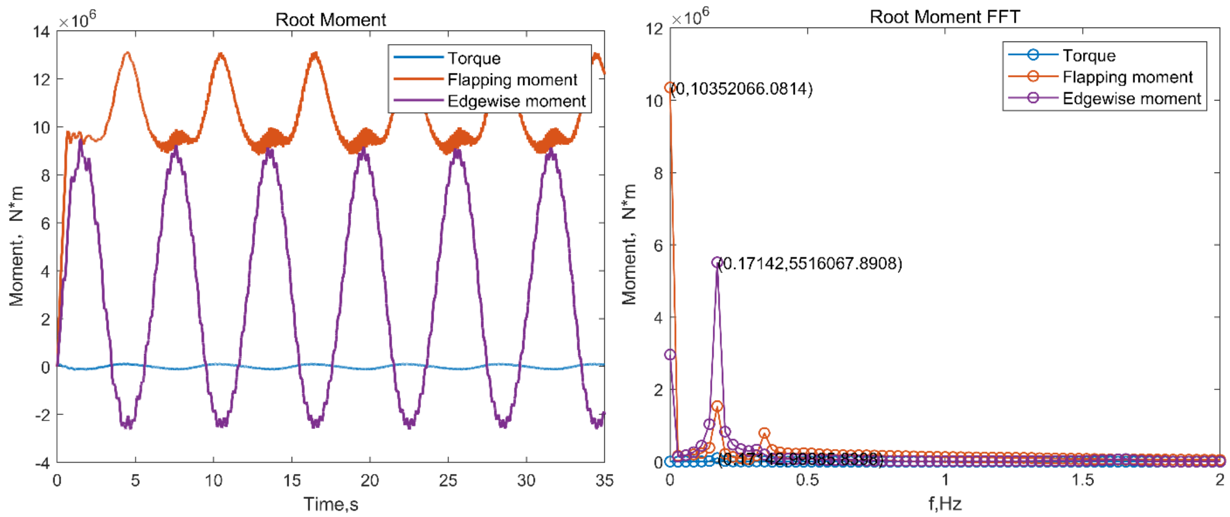

（a） (b)

Fig. 11 （a）Time-domain response of root moment;(b)FFT results of root moment

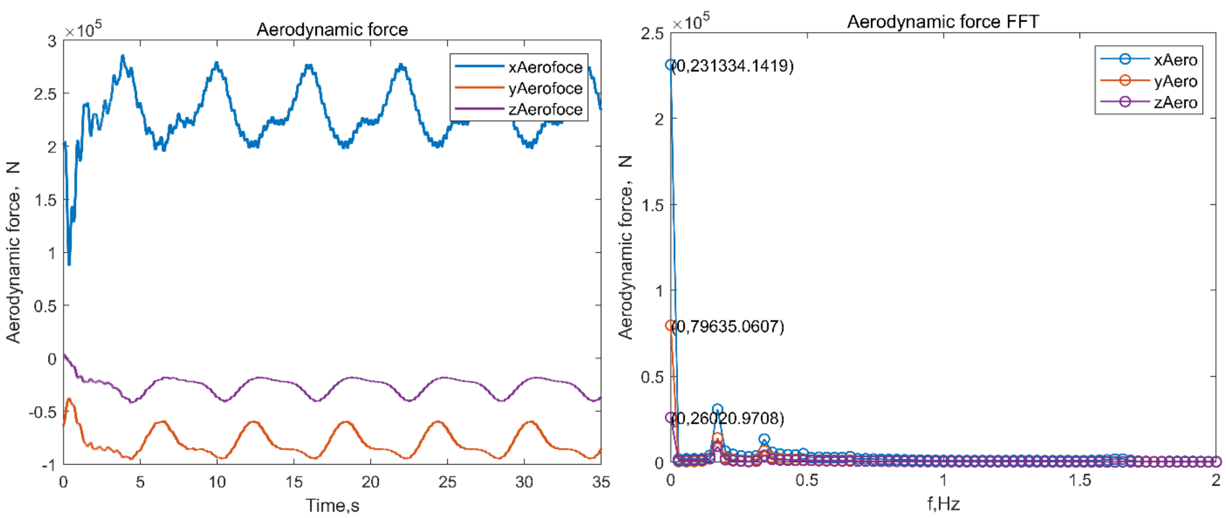

（a） (b)

Fig. 12 （a）Time-domain response of aerodynamic force; (b)FFT results of aerodynamic force

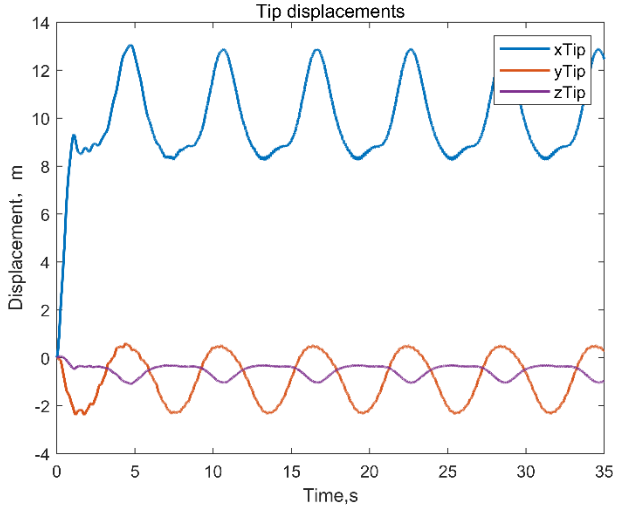

(a)

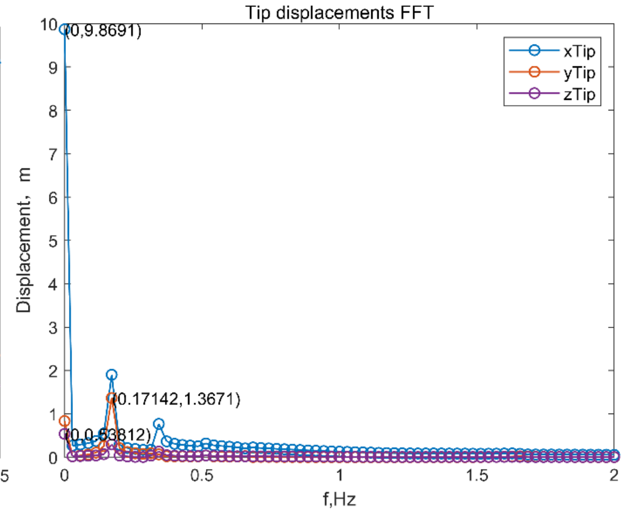

(b)

Fig. 13 （a）Time-domain response of tip displacements; (b)FFT results of tip displacements

Table 3 Magnitudes in FFT results at frequency equals to zero

Case No.	**CASE1**	**CASE 2**	**CASE 3**	**CASE 4**	**CASE 5**
X-force,N	2.31E+05	2.29E+05	2.88E+05	2.51E+05	2.27E+05
Y-force,N	7.96E+04	7.82E+04	7.79E+04	7.01E+04	7.77E+04
Z-force,N	2.60E+04	2.54E+04	4.87E+04	3.53E+04	2.55E+04
Torsion,N·m	4.33E+03	4.64E+03	3.68E+04	1.46E+04	1.88E+03
Flapping moment, N·m	**1.04E+07**	**1.03E+07**	**1.33E+07**	**1.15E+07**	**1.02E+07**
Edgewise moment, N·m	2.96E+06	2.91E+06	3.14E+06	2.76E+06	2.90E+06
X-Dis,m	9.87	9.80	13.41	11.57	9.77
Y-Dis,m	0.83	0.82	0.99	0.84	0.82
Z-Dis,m	0.54	0.52	1.23	0.84	0.53

Table 4 Magnitudes in FFT results at frequency equals to 0.17Hz

Case No.	CASE1	CASE 2	CASE 3	CASE 4	CASE 5
X-force,N	3.08E+04	2.76E+04	2.68E+04	2.97E+04	3.70E+04
Y-force,N	1.41E+04	1.27E+04	1.06E+04	1.09E+04	1.65E+04
Z-force,N	9.19E+03	7.70E+03	1.35E+04	1.15E+04	1.08E+04
Torsion,N·m	9.99E+04	1.03E+05	1.34E+05	1.18E+05	9.56E+04
Flapping moment, N·m	1.54E+06	1.20E+06	1.53E+06	1.61E+06	1.94E+06
Edgewise moment, N·m	5.52E+06	5.69E+06	5.61E+06	5.59E+06	5.34E+06
X-Dis,m	1.90	1.66	2.02	2.02	2.18
Y-Dis,m	1.37	1.41	1.48	1.44	1.33
Z-Dis,m	0.29	0.25	0.48	0.39	0.34

4 CONCLUSIONS

In this work, a nonlinear aeroelastic formulation for large wind turbine blade has been established. The strain-based nonlinear beam model considering rotational effects is derived for structural modelling. The unsteady aerodynamic loads are calculated by the finite-state inflow theory. A typical blade model was numerically investigated and the results were compared to the measured data. The results indicate that the proposed model can simulate the nonlinear aeroelastic response of blades. It can to some extent capture the atypical vibration characteristics of flexible blades. However, there is still a significant error between the current results and the measured data. On one hand, there may be a lack of consideration for stall characteristics in aerodynamic modeling, and on the other hand, it is necessary to integrate more measurement data for evaluation, such as vibration acceleration signals.

REFERENCES

[1]. Jahani K , Langlois R G , Afagh F F .Structural dynamics of offshore Wind Turbines: A review.Ocean engineering, 2022:251.

[2]. Voormeeren, S.N., Van Der Valk, P.L.C., Rixen, D.J., Practical aspects of dynamic substructuring in wind turbine engineering. Proceedings of the Society for Experimental Mechanics Series. Springer New York LLC, 2011: 163–185.

[3]. Voutsinas, S.G.. Structural Dynamics of Wind Turbines, 2010: 121–151.

[4]. Gupta, S., Leishman, J.G., Dynamic stall modelling of the S809 aerofoil and comparison with experiments. Wind Energy 2006,9: 521–547.

[5]. Jeon, M., Lee, Soogab, Kim, T., Lee, Seunghoon, Wake influence on dynamic load characteristics of offshore floating wind turbines. AIAA J 2016, 54, 3535–3545.

[6]. Volk, D.M., Kallesoe, B.S., Johnson, S., Pirrung, G.R., Riva, R., Barnaud, F.. Large wind turbine edge instability field validation. In: Journal of Physics: Conference Series. IOP Publishing Ltd. 2020.

[7]. Kallesøe, B.S.. Effect of steady deflections on the aeroelastic stability of a turbine blade. Wind Energy 2011, 14: 209–224.
[8]. Zhou, X., Huang, K., Li, Z.. Effects of bend-twist coupling on flutter limits of composite wind turbine blades. Compos. Struct. 2018, 192: 317–326.
[9]. J. C. SIMO, L. VU-QUOC. A three-dimensional finite-strain rod model. Part II: Computational aspects. Computer Methods in Applied Mechanics and Engineering. 1986(58): 79-116.
[10]. Weihua Su, Carlos E. S. Cesnik. Strain-based geometrically nonlinear beam formulation for modeling very flexible aircraft. International Journal of Solids and Structures. 2011; 48(16): 2349-2360.
[11]. Peters, D.A.,Karunamoorthy, S., Cao, W.M., Finite State Induced Flow Models Part 1: Two-Dimensional Thin Airfoil, Journal of Aircraft, 32(2),1995
[12]. Hodges D.H. and Pierce G.A, Introduction to Structural Dynamics and Aeroelasticity, Cambridge University Press, 2002
[13]. Géradin M, Rixen DJ. Mechanical vibrations theory and application to structural dynamics. 3rd ed. New York: John Wiley & Sons;1997.p.564-8.